

Continuous-Wave and Time-Resolved Optically Detected Magnetic Resonance Studies of Nonetched/Etched InP Nanocrystals

L. Langof, E. Ehrenfreund, and E. Lifshitz*

Solid State Institute, Technion-Israel Institute of Technology, Haifa 32000, Israel

O. I. Micic and A. J. Nozik

National Renewable Energy Laboratory, Golden, Colorado 80401

Received: October 4, 2001

The low temperature photoluminescence spectrum of InP nanocrystals (NCs) is composed of a near band-edge exciton and a defect emission band at lower energies. The present study characterized the defect emission utilizing an optically detected magnetic resonance spectroscopy (ODMR) both in continuous-wave and time-resolved modes. The continuous-wave ODMR spectra were measured as a function of the laser power, the microwave power, the microwave modulation frequencies, and of the light polarization. The results showed that the defect emission originated from the trap-to-band luminescence of a weakly coupled electron–hole pair, when the electron is trapped at a phosphorus vacancy, V_p (with angular momentum of $F = 1/2$), while the hole is located at the valence band (with $F = 3/2$). Spin Hamiltonian simulations of the ODMR lineshape, including hyperfine interactions, revealed that the nonetched samples are dominated by V_p at the surface with two adjacent indium atoms. While treatment with hydrogen fluoride acid eliminates the surface defects, it leaves behind a small percent of V_p at the core of the NCs, with four indium atoms next neighbors at the vertexes of a tetrahedral site. The time-resolved ODMR measurements further distinguished between radiative and nonradiative processes and followed the spin dynamics at the excited state. Kinetic simulations of the PL intensity response to a microwave square wave modulation indicated that the spin–lattice relaxation time and the radiative lifetime of the weakly coupled electron–hole pair are in the microseconds regime.

Introduction

In recent years, there has been an increase of interest in the scientific and technological aspects of colloidal semiconductor nanocrystals (NCs). These materials exhibit unique chemical and physical properties, differing substantially from those of the corresponding bulk solids.^{1–6} The special properties are associated with the quantum size effect and the control of surface quality. The impact of the quantum size effect in the III–V NCs is of a special interest, due to their large exciton Bohr radius (10–34 nm) and relatively narrow band gap (0.4–1.5 eV).¹⁹ In such a case, the Bohr radius exceeds the NC diameter, which in turn leads to strong confinement of carriers and a relatively large blue shift of the band edge.

The successful preparation of colloidal suspensions of InP⁷ and InAs⁸ has been achieved in recent years. The colloidal method permits the growth of NCs with controlled diameters of <10 nm that exhibit a high degree of reproducibility, a relatively narrow size distribution (<10%), a uniform shape, and offer the possibility to modify the surface.^{9,10} Furthermore, colloid NCs shows a large offset of the states with respect to the vacuum and thus a large confinement of electron and hole states.¹¹ For example, colloidal InP NCs (diameters 2.5 and 6.0 nm) showed steplike absorption spectra that are blue-shifted up to 1 eV with respect to the bulk material.⁷ The PL-excitation (PLE) spectra of nearly monodispersed particles of InP¹² and InAs,¹³ passivated with organic capping agents, exhibited about nine electronic transitions associated with the existence of quantized states, having different total angular momentum. The atomic-like nature of these high-quality NCs has been proven

by fluorescence line narrowing (FLN),¹⁴ size-selective PLE,¹² and single-NC luminescence spectroscopy.¹⁵

The theoretical aspects of the quantum size effect and electronic properties of individual InP and InAs NCs have been treated in several major publications.^{12,13,16,19} The traditional approach utilized the $k \cdot p$ method, in which NC wave functions are expanded in terms of a small number of Γ -like bulk band-edge states, independent Coulomb interactions and constant bulk dielectric screening. In addition, electron–hole exchange interaction was included, which led to 6×6^{12} and 8×8^{13} mixing of the valence or valence-conduction bands, respectively. This approach anticipated several excitonic transitions among quantized states with spin polarities. For example, this method indicated that the two lowest transitions, $1p_{3/2} - 1S_e$ and $1p_{1/2} - 1S_e$, are dipole forbidden, whereas the lowest allowed transition is $1S_{3/2} - 1S_e$. A more recent approach utilized an atomistic pseudo-potential method. The latter approach utilized a dependent Coulomb interaction with position-dependent dielectric screening.^{16,19} This method indicated that single-NC states do not have purely odd or even angular-momentum envelope parity and that the lowest energy-states in small NCs originates from the L-point in the Brillouin-zone. Furthermore, this approach allows the $1S_{3/2} - 1S_e$ to be the lowest energy transition.

Although carrier confinement in colloidal III–V NCs is expected to lead to enhanced PL efficiency, this is not frequently observed, presumably due to the trapping of carriers at the surface and nonradiative recombination. Indeed, Micic et al.¹⁷ showed that the growth of InP colloidal NCs under excess indium produces a red luminescence band, while the growth

under excess phosphorus eliminates this band. Furthermore, etching of the samples with hydrogen fluoride acid (HF) partially quenches the red luminescence from surface traps. This suggests that the red band corresponds to stoichiometric defects at the surface. Time-resolved spectroscopy showed nonlinear bleaching of the exciton band, persisting for about 500 ns, probably due to trapping at surface states.^{14,17} Poles et al.¹⁸ showed anti-Stokes PL (PL up-conversion) spectra of colloidal InP NCs. They assigned the anti-Stokes transitions to a phonon-assisted recombination between surface and band edge states. Fu and Zunger¹⁹ suggested that those surface states are associated with indium and phosphorus dangling bonds; however, at the current time there is no explicit identification of those sites.

Thus, the ultimate goal of this work is concerned with the identification of the surface trapping sites and their influence on the recombination processes. Colloidal InP NCs, capped with organic ligands were prepared by wet chemical methods, while their surfaces were treated by several etching procedures. Continuous-wave and time-resolved optically detected magnetic resonance (cw ODMR and TR-ODMR) spectroscopy was used for the study of the surface properties. The ODMR method provided the means to chemically identify surface/interface sites, correlated them with the specific optical transition and revealed information about the exchange interaction between trapped electrons and holes. In the TR-ODMR reported here we utilized the pulsed microwave technique, enabling one to distinguish between radiative and nonradiative characteristics of a trapping site and to evaluate the spin-lattice relaxation time.

Experimental Section

Synthesis and Structural Characterization. InP NCs were synthesized by colloidal chemistry methods, using an indium chloride (InCl_3) and tris-(trimethyl-silyl)phosphine ($\text{P}(\text{SiMe}_3)_3$) as the starting reactants. These reactants were heated for 3 days at 260–280 °C in the presence of trioctylphosphine oxide (TOPO) and trioctylphosphine (TOP). The synthesis was conducted in rigorous air-free and water-free atmospheres. Under those conditions, TOPO/TOP produced compact hydrophobic capping of the NC surface. A detailed description of the preparation procedure is given in refs 17 and 20. Fractionation of the NCs into different sizes was achieved through the selective precipitation method, described by Murray et al.²¹ This procedure led to a size distribution of about 10%. This stabilizer enables one to redissolve the NCs and embed them in polymer films, suitable for the optical and magnetic resonance measurements indicated below.

Previous experience showed that intense band edge emission (with quantum yield up to 40%) is achieved after etching of the NCs²⁰ with HF. A two-liquid-phases etching procedure was used. The two-phase system was formed by mixing 1–10 μL of a butanol solution containing 5% HF and 10% H_2O , with 4 mL of a colloidal solution containing hexane, butanol, acetonitrile (1:0.1:1), 2–5% TOPO, and InP NCs. The NCs should have been dispersed in the lower density nonpolar hexane phase, while the HF, butanol, and water remained in the acetonitrile phase. This ensured that the etching rate was slow and uniform. The mixture was shaken, left overnight and then the hexane phase containing the NCs was separated and used. Relatively low concentrations of HF and fresh colloidal InP NC solutions were required.

Instrumental. In the cw ODMR experiment, we monitored a change in luminescence intensity, ΔI_{PL} , resulting from a magnetic resonance event at the excited state. Thus, a plot of ΔI_{PL} versus the strength of an applied external magnetic field,

B , during a simultaneous application of a microwave (MW) radiation, led to an electron spin resonance-like spectrum. The cw ODMR spectra were recorded by immersing the sample in a cryogenic Dewar (1.4K), centered within a High-Q resonance cavity (at the area of maximal magnetic field component), coupled to a MW source ($\nu_{\text{MW}} = 10.8 \text{ GHz}$), and surrounded by a superconducting magnet ($B = 0.0\text{--}3.0 \text{ T}$). The MW output power was square-wave modulated at frequencies between 0.1 and 1.5 kHz, while the induced change in the luminescence was measured by a lock-in detection, synchronized with the MW modulation frequency. The samples were excited with a continuous Ar⁺ laser, while the emitted light was passed through a holographic grating monochromator or cutoff color filters and detected by Si detector. The emitted beam was detected in either of the following directions: (a) parallel to the external magnetic field (Faraday configuration) or (b) perpendicular to it (Voigt configuration). A total emission or a circular-polarization component (σ^+ or σ^-) was detected in both configurations.

The time-resolved ODMR (TR-ODMR) could be carried out either under light transient, or MW transient measurements. In the light transient measurement, the excited laser beam was pulsed using an acousto-optic modulator (with 40 ns rise time) and a chosen repetition rate. A boxcar analyzer measured the TR luminescence, while its spin dependence was measured by applying a MW pulse at a frequency doubled of that of the excited light. Thus, the luminescence intensity with and without a MW were subtracted from one another at various delay times beyond the laser pulse. In the MW transient measurement, the excited laser beam was continuous, while the variation in the luminescence intensity during and after a microwave pulse was recorded. This direct spin-dependence was recorded with a boxcar analyzer, as will be shown in the next section. It should be noted that the light transient measurement gave extremely weak signals, while the MW transient detection was found to be more suitable for the current study.

Results

The photoluminescence (PL) spectra of nonetched (with average diameter of 4.4 nm) and HF etched InP NCs, are shown by the dashed lines in Figure 1, parts a and b, respectively. The PL spectrum of the etched sample is dominated by an exciton band centered at $\sim 2 \text{ eV}$, and accompanied by a weak tail at the low energy side. On the contrary, the nonetched sample is dominated by a deep broad band centered at 1.5 eV, with a full width half-maximum (fwhm) of 0.2 eV, and a weak exciton shoulder at 1.8 eV. It should be noted that the etching process strips one or two monolayers of InP from the external surface, which reduces the NCs size and leads to a shift of the exciton band. A magnetic resonance effect was absent when detecting at the exciton spectral regime. However, a pronounced change in luminescence intensity ($\Delta I_{\text{PL}}/I = 0.5\%$) was observed upon the application of the magnetic resonance conditions (external magnetic field and MW radiation at a fixed frequency) when detected at the spectral regime below 1.8 eV. Thus, the cw ODMR spectra of a non-exciton process, recorded at the Faraday configuration with linear detection, of the etched and nonetched samples, are shown in Figure 2 by the dashed and solid curves, respectively. Both cases consist of a single positive resonance, centered at 0.40 T in case of a nonetched sample, and 0.39 T in case of an etched sample, with fwhm of 0.07 and 0.1 T, respectively. However, the resonance intensity of the etched sample is about 100 times weaker than that of the nonetched sample. The ODMR spectral dependence curves of both samples

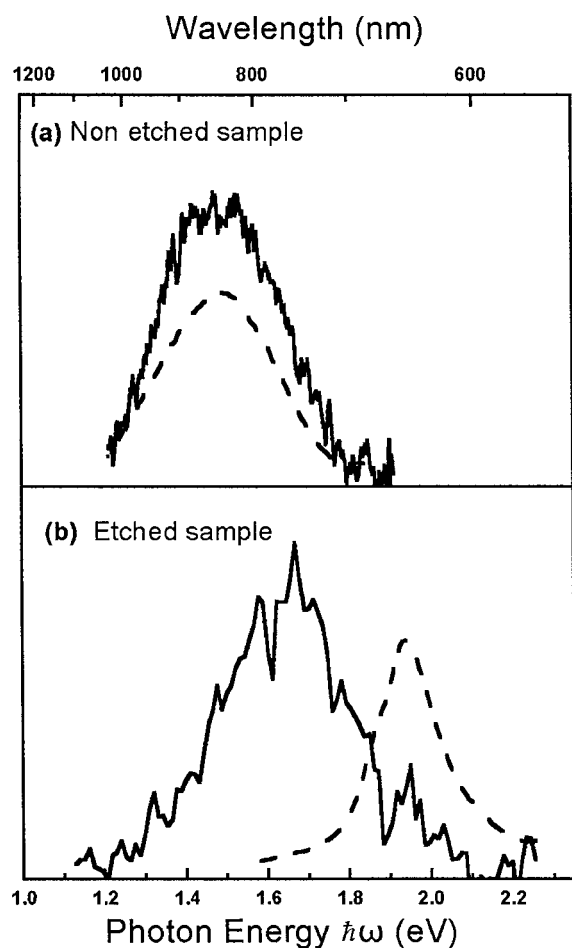


Figure 1. The photoluminescence spectra of nonetched and HF etched InP NCs (dashed line), and spectrally dependent ODMR spectra (solid line).

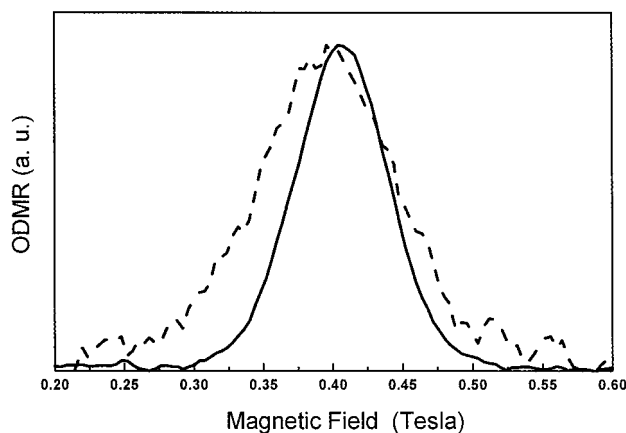


Figure 2. ODMR spectra of HF etched (dashed line) and nonetched (solid line) InP NCs.

are shown in Figure 1 by the solid lines. They were recorded by scanning the change in PL intensity versus emission energy during an application of the resonance conditions, with an external magnetic field of 0.4 T and MW radiation of $\nu_{\text{MW}} = 10.8$ GHz. Both samples showed a spectral dependent ODMR band, which ranged between 1.2 and 2.0 eV, covering the entire nonexciton regime. In fact, this spectral dependence solely coincides with the PL spectrum of the nonetched sample, but deviates from the exciton band of the etched sample.

Representative cw ODMR spectra of the nonetched sample, recorded with circular polarizer in Voight and Faraday con-

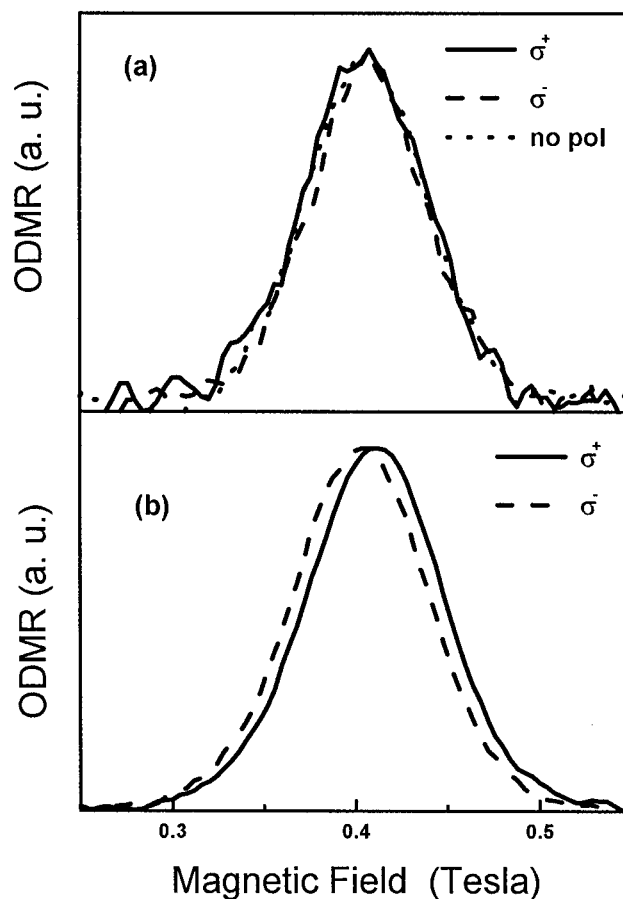


Figure 3. ODMR spectra of the nonetched sample, recorded with the circular polarizer in Voight (a) and Faraday (b) configurations.

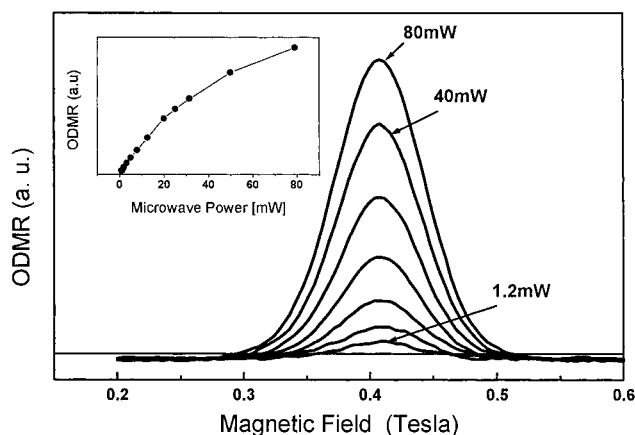


Figure 4. The ODMR spectra recorded at various MW power outputs. Inset: ODMR band intensity as a function of MW power.

figurations, are shown in Figures 3, parts a and b, respectively. The σ^+ and σ^- detection in the Faraday configuration showed a similar resonant bands, however they were shifted one with respect to the other by about 0.008 T. However, the circular polarized components are indistinguishable at the Voight configuration.

The cw ODMR spectra (linear or circular polarized) recorded at various MW power output, ranging between 0.5 and 75 mW, are shown in Figure 4, while the integrated intensity dependence on the MW power is plotted at the inset of the figure. The latter indicates that the intensity of the ODMR band increases but does not reach a plateau at the highest MW powers.

The cw ODMR spectra, recorded at various MW modulation frequencies, in-phase with the MW square wave, are shown in

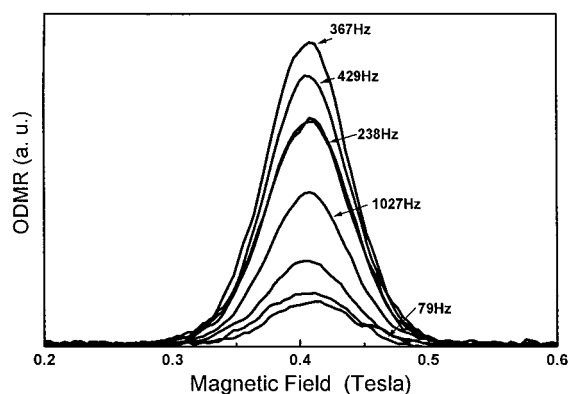


Figure 5. The ODMR spectra recorded at various MW modulation frequencies.

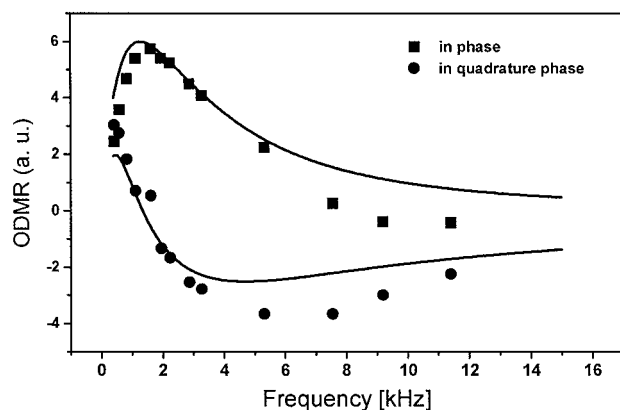


Figure 6. The plot of integrated intensity of the ODMR versus the MW modulation frequency, when recorded in-phase and at a quadrature phase with the MW square wave.

Figure 5. The plot of the integrated intensity of the ODMR band, versus the MW modulation frequency, when recorded in-phase and at a quadrature phase with the MW square wave, is given by the dots in Figure 6. It is seen from the figure that, at the in-phase detection, the intensity increases slightly, up to a frequency of 2 kHz, and then decreases gradually with any further increase of the MW modulation. The quadrature dependence decreases gradually with the increase in the frequency until 4.5 kHz, followed by a slight increase with further increase of the MW modulation beyond 4.5 kHz. The aforementioned frequency response will be compared below with the time-resolved experiments. Furthermore, the solid lines in Figure 6 show a theoretical fit, which will be discussed in the next section.

The TR-ODMR spectrum of the nonetched sample, obtained with a MW transient measurement, is shown in Figure 7 by the noisy line. The solid line corresponds to a theoretical fit (vide infra), while the corresponding MW pulse is shown below the spectrum. This spectrum shows an instant spike of the luminescence intensity at the rising edge of the MW pulse, followed by an intensity decay, then by a sudden negative drop at the falling edge of the MW pulse, and finally, by a recovery to a steady-state intensity. The spin dynamics associated with this sequence of changes will be given in the Discussion.

Discussion

The PL of the etched sample is characterized by an exciton luminescence, accompanied by a tail, presumably associated with a stoichiometric defect recombination. As mentioned in the Introduction, chemical treatment of the samples with excess

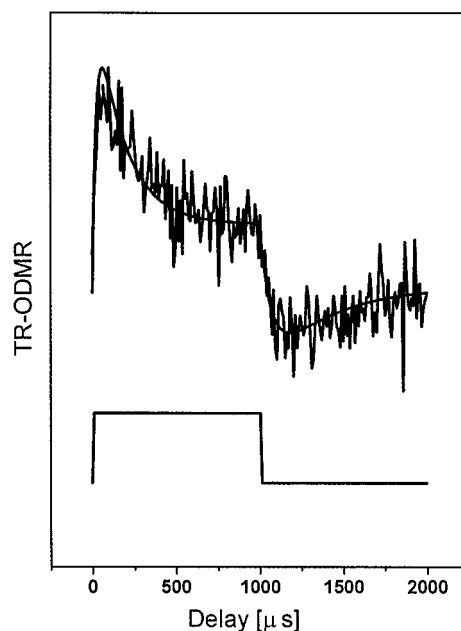


Figure 7. The TR-ODMR spectrum of non-etched sample, obtained with a MW transient measurement.

phosphorus during the growth or post HF etching reduces the tail recombination and enhances the exciton efficiency. Indeed, the defect recombination band dominates the PL of nonetched sample. The ODMR spectral dependence coincides solely with the defect luminescence band, and thus, the magnetic resonance phenomena discussed below determine the nature of this recombination (trap-to-trap or trap-to-band), chemical identification of a defect site, electron-hole (e-h) exchange interaction and the spin dynamics.

The ODMR spectra shown in Figures 2 and 3, are associated with a spin flip at the excited state of either an electron, a hole or both. It is assumed that the electron and hole have unpaired spins of $S_e = 1/2$ and $S_h = 1/2$, an angular momentum of $L_e = 0$ and $L_h = 0, 1$ and a spin-orbit of $F = S + L$. The projections of F in the direction of an external magnetic field ($B||z$) have the values of $m_{Fe} = \pm 1/2$ and $m_{Fh} = \pm 3/2, \pm 1/2$. These projections split in the presence of an external magnetic field by a Zeeman interaction, $\beta g^{\text{iso}} B$ (β and g^{iso} are the Bohr magneton and isotropic g spectroscopic factor, respectively). The spin-orbit configuration at the excited state may exhibit either one of the cases, shown schematically in Figure 8. The label J in the figure corresponds to an isotropic e-h exchange interaction, while D corresponds to a zero-field splitting. The corresponding ODMR spectra depend on the spin selection rules, conservation of angular momentum and on the ratio between the radiative lifetime (τ_{rad}) and the spin-lattice relaxation time (T_1).

Case a, shown in Figure 8, consists of a 4-fold spin-manifold, associated with $F_e = 1/2$ and $F_h = 1/2$ and a weak e-h exchange interaction ($J \ll \beta g^{\text{iso}} B$). An optical excitation creates an isotropic spin distribution; however, if $\tau_{\text{rad}} \ll T_1$ (unthermalized case) the population of the $|\pm 1/2, \mp 1/2\rangle$ states (with $\Sigma F = 0$) is reduced rapidly by radiative transitions to the ground state, as shown by the dashed arrows in the Figure 8. This radiative process has a linear polarization both in the Faraday and the Voigt configurations. Then, the application of a MW power at resonance with the $\Delta m_F = \pm 1$ transitions (shown by the solid arrows in the figure) restores an isotropic spin distribution and enhances the luminescence intensity from the $\Sigma F = 0$ spin states. An anticipated ODMR spectrum of case a is shown schematically below the spin diagram. It consists of two

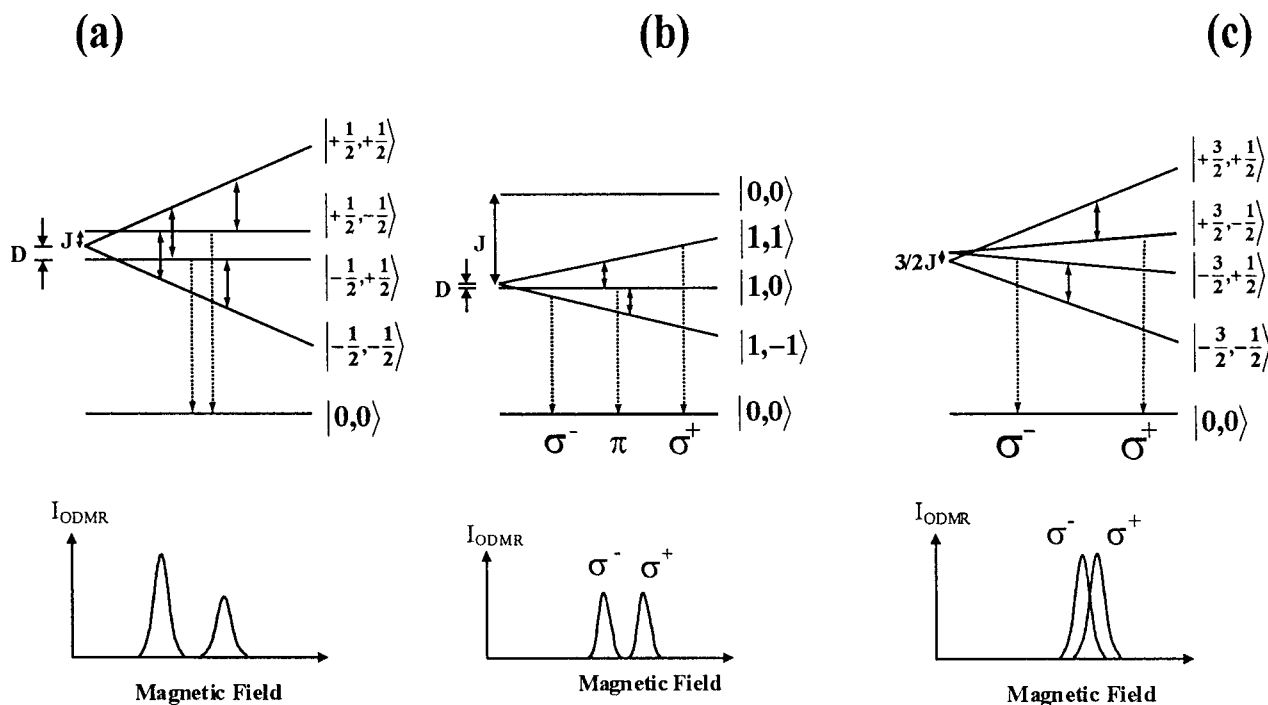


Figure 8. Different spin orbit configurations at the excited state and the corresponding ODMR spectra.

resonance bands, corresponding to the spin flip of an electron and a hole. Each band can be split (or widened) by an exchange, or by an electron spin–nuclear spin (hyperfine) interaction.²² If $\tau_{\text{rad}} \geq T_1$, thermalization occurs prior to the radiative process, creating a Boltzmann distribution population among the spin manifold. In such a case, two $\Delta m_F = -1$ transitions, shown in diagram a, reverse their signs, leading to a quenching of the luminescence intensity and to negative ODMR bands (not shown).²³

Case b of Figure 8 represents a spin diagram of $F_e = 1/2$ and $F_h = 1/2$ with $J \gg \beta g^{\text{iso}} B$. A bound exciton is characterized by a strong exchange interaction. Due to the localization nature of such an exciton, the angular quantum momentum L_h may be quenched, and thus, $F \sim S$, forming a singlet ($|1,0\rangle$) and triplet ($|1, \pm 1\rangle$, $|1, 0\rangle$) states. Furthermore, the $|0,0\rangle$ state populates the $|1,0\rangle$ nonradiatively, enhancing the $|1,0\rangle \rightarrow |1, \pm 1\rangle$ resonance transitions. Then, the conservation of an angular momentum enables a circularly polarized radiative recombination from the triplet $|1, \pm 1\rangle$ states in the Faraday configuration. An anticipated spectrum is drawn below diagram (b). The ODMR spectrum in the Faraday configuration consists of a single positive band, with separation between the σ^+ and σ^- of D. Under the Voigt configuration emission is detected from the entire spin manifold, therefore, the $|1,0\rangle \rightarrow |1, \pm 1\rangle$ magnetic transition quenches the luminescence leading to a negative ODMR band (not shown).

Case 8c consists of a 4-fold spin-manifold, associated with $F_e = 1/2$ and $F_h = 3/2$ and a weak exchange interaction. According to an angular momentum conservation law, the $|\pm 3/2, \mp 1/2\rangle$ states can recombine radiatively with circular polarization (σ^+ and σ^-) at the Faraday configuration. Furthermore, magnetic resonance transitions occur from the $|\pm 3/2, \pm 1/2\rangle$ nonradiative to the radiative spin states, leading to a spin flip of the sole electron and to an enhancement of the luminescence intensity. For an unthermalized condition it is anticipated that the ODMR spectrum will consist of a single ODMR band (either in the left or right circular direction), that can be further broadened by exchange or hyperfine interactions (shown below diagram 8c). It should be noted that the detection

of the ODMR signal in the transverse direction (Voigt configuration) comprises of a positive contribution from both the left and right circular components, making them indistinguishable.

The experimental ODMR spectra, shown in Figures 2 and 3 showed the existence of a single positive band, both in the Faraday and Voigt configurations, which could be fitted to a single Gaussian function. Furthermore, both the left and right circular detection showed an enhancement of the luminescence intensity, with a mutual shift of about 0.008 T in the Faraday configuration. This is in contradiction with the anticipation of two independent resonance bands for weakly coupled electron and hole (case a), or a creation of a bound exciton (case b) with a negative band in the Voigt configuration. Consequently, these spin configurations can be excluded. Instead, the experimental evidence supports the occurrence of magnetic resonance transitions, associated with $F_e = 1/2$ and $F_h = 3/2$ spin system shown in Figure 8, part c. This resonance band can be simulated with the following spin Hamiltonian:²²

$$H_s = \beta g_e S_e H + \beta g_h S_h H + J S_e S_h + S_e D S_h + S_e A I_n \quad (1)$$

The first two terms in the Hamiltonian corresponds to the electron and hole Zeeman interaction. The third and fourth terms consist of the isotropic e–h exchange and the zero-field splitting, respectively. The fifth term corresponds to a hyperfine interaction with the surrounding nuclei. For random orientation of e–h pair dipoles, the zero-field splitting is average to zero. Then, with an initial assumption of a zero hyperfine interaction, the diagonalization of the spin Hamiltonian leads to the following spin levels' energies:

$$\begin{aligned} E(|+\frac{3}{2}, +\frac{1}{2}\rangle) &= \frac{1}{2}\beta g_e H + \frac{3}{2}\beta g_h H + \frac{3}{4}J \\ E(|+\frac{3}{2}, -\frac{1}{2}\rangle) &= -\frac{1}{2}\beta g_e H + \frac{3}{2}\beta g_h H - \frac{3}{4}J \\ E(|-\frac{3}{2}, +\frac{1}{2}\rangle) &= \frac{1}{2}\beta g_e H - \frac{3}{2}\beta g_h H - \frac{3}{4}J \\ E(|-\frac{3}{2}, -\frac{1}{2}\rangle) &= -\frac{1}{2}\beta g_e H - \frac{3}{2}\beta g_h H + \frac{3}{4}J \end{aligned} \quad (2)$$

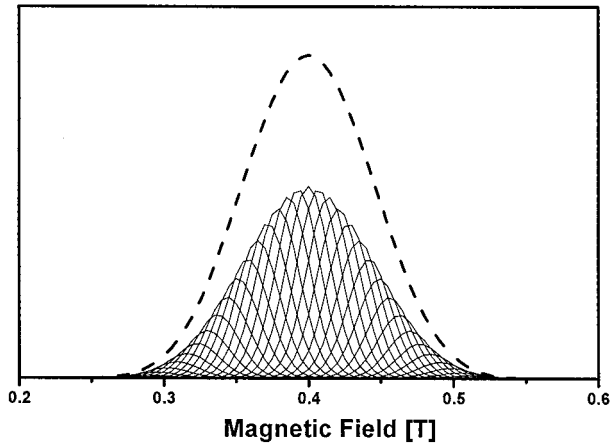


Figure 9. The simulated ODMR lineshape resulting from hyperfine interaction with four nearest neighbors.

Considering a sole spin flipping of electrons, the ODMR band, shown in Figure 2, could be fitted to a theoretical curve with $g_e = 1.93$ and $J = 0.28 \mu\text{eV}$ for a nonetched sample, and $g_e = 1.98$ for an etched sample. The increase in the g factor in the etched sample may arise from a confinement effect, due to the reduction of the NCs size upon etching (as indicated in the Results) or due to the existence of a different crystallographic defect. However, an influence of a size effect on the g value was recently suggested by Efros et al.²⁴ for CdSe NCs. The J value was derived from the mutual shift of the σ^+ and σ^- spectra shown in Figure 3, part a. However, the indicated g and J values with an intrinsic line broadening led to a resonance band with fwhm of about 0.03 T, substantially smaller than the observed width. The experimental line shape could be simulated only by addition of hyperfine interactions between the trapped electron with the surrounding indium nuclei. The indium atom has a nuclear spin of $I = 9/2$ with neutral abundance of 100%, while a hyperfine interaction with n next neighbors should lead to $2nI + 1$ subbands. Representative subbands for $n = 4$ are shown by the thin solid lines in Figure 9. However, since the indium isotropic hyperfine constant is 390 MHz,²⁵ and the sample is studied as a power pattern, the detailed hyperfine lines cannot be resolved and instead, this coupling contributes to the broadening of the studied resonance band. It was shown before that the hyperfine broadening leads to a Gaussian line shape,²⁵ similar to the band observed in the present case. Hyperfine interaction with four indium nuclei reveals that the electron is trapped at a phosphorus vacancy, surrounded by the neighboring indium atom of a tetrahedral site, leading to a broadening of about 0.098 T, as shown by the dashed line in Figure 9. However, phosphorus vacancy at the surface may have only two indium neighbors, leading to a broadening of only 0.067 T. In fact the etched sample line shape can be fitted with the interaction of four indium atoms, while the ODMR band of the nonetched samples is fitted by an interaction with two indium atoms. This distinction suggests that the nonetched sample exhibits surface phosphorus vacancies. The latter fills the stoichiometric defects, while surface treatment with HF molecules may also substitute the vacant phosphorus atoms. The spectral dependence ODMR curves, shown in Figure 1, indicate that the entire nonexciton band or tail correspond to a recombination between a trapped electron at a phosphorus vacancy with a heavy hole (with $F = 3/2$) in the valence band. The extended wave function of the hole enabled a reasonable overlapped with the trapped carrier and indeed an e–h exchange interaction in the deviate from the exchange value of an exciton (30 meV) and resemble the value which was found recently for

trapped electron-trapped hole recombination ($0.2 \mu\text{eV}$) in colloidal NCs.²² The magnitude of the exchange interaction is proportional to the overlap integral of the wave function of both carriers and is given by²⁶

$$J = J_0 \exp(-2r/r_0) \quad (3)$$

where r_0 is the Bohr radius of the wave function of the less localized carrier and r is the separation between the interacting carriers. J_0 should be similar to the size of the exchange of an exciton. It is reasonable to assume that r is close to the radius of the NCs and thus may deviate from a single value due to the existence of a $\sim 10\%$ distribution in the NCs size. The g_e value of the electron deviates considerably from that of a reported bulk value of $g_e = 1.15$ – 1.5 at the conduction band,²⁷ however, the observed g_e value does not approach the free electron $g_e = 2.0$. This suggest that the electron is trapped at a phosphorus vacancy, but is slightly delocalized over the first next indium neighbors, pronounced by the hyperfine broadening.

The time-resolved ODMR measurement further clarifies the spin dynamics and characteristics of the magnetic sites (radiative versus nonradiative). Assuming that saturation of the spin levels is avoided (based on the measurement shown in Figure 4), the spin kinetic processes of the $|+3/2, -1/2\rangle$ and $|+3/2, +1/2\rangle$, or $|-3/2, -1/2\rangle$ and $|-3/2, +1/2\rangle$ pair states, shown in Figure 8, part c, are given by the following equations:

$$\frac{dn_1}{dt} = -\frac{n_1}{\tau_1} + G - \frac{n_1 - (n_1 + n_2)(1 - \rho)}{T_1} - (n_1 - n_2)P_{\text{MW}} \quad (4a)$$

$$\frac{dn_2}{dt} = -\frac{n_2}{\tau_2} + G - \frac{n_2 - (n_1 + n_2)\rho}{T_1} - (n_2 - n_1)P_{\text{MW}} \quad (4b)$$

$$\rho = \frac{1}{1 + \exp(\Delta E/kT)}, \quad \Delta E = h\nu_{\text{MW}} \quad (4c)$$

where n_1 and n_2 correspond to the populations of a single pair states. G corresponds to the generation rate, while τ_1 and τ_2 are the corresponding decay times (when $\tau^{-1} = \tau_{\text{rad}}^{-1} + \tau_{\text{nr}}^{-1}$, rad and nr correspond to the radiative and nonradiative processes). T_1 is the spin–lattice relaxation, while P_{MW} corresponds to the MW power. The analytical solution of four kinetic equations (with $P_{\text{MW}} = 0$ and $P_{\text{MW}} \neq 0$) yields a theoretical change in the PL intensity due to a magnetic resonance between two states, induced by a square-wave modulation of the MW power, as shown in Figure 10. Curve a in the figure agrees with a radiative recombination from two spin states with $\tau^{-1} \approx \tau_{\text{rad}}^{-1}$ and $\tau \ll T_1$ (unthermalized). This curve is compared with the MW pulse response, shown at the bottom of the figure. The radiative process shows a strong spike at the rising edge and a sudden drop at the end of the pulse. Curve b corresponds to a radiative processes from both spin states competing with nonradiative processes and $\tau_{\text{rad}} \approx T_1$. The intensity response also starts with a spike, which decays gradually until the end of the pulse, followed by a negative spike after the pulse, however the latter recovery gradually goes down to zero intensity. Case c involves competing radiative and nonradiative processes, but radiative emission from one of the states is dominated and $\tau_{\text{rad}} \ll T_1$ (unthermalized). The response shows a small positive change of the PL intensity at the rising edge and a small negative change at the falling edge. Curve d includes similar radiative and nonradiative decay times to those in case c; however, $\tau_{\text{rad}} > T_1$ (thermalized), leading to a Boltzmann population distribution. The later distribution reserves the

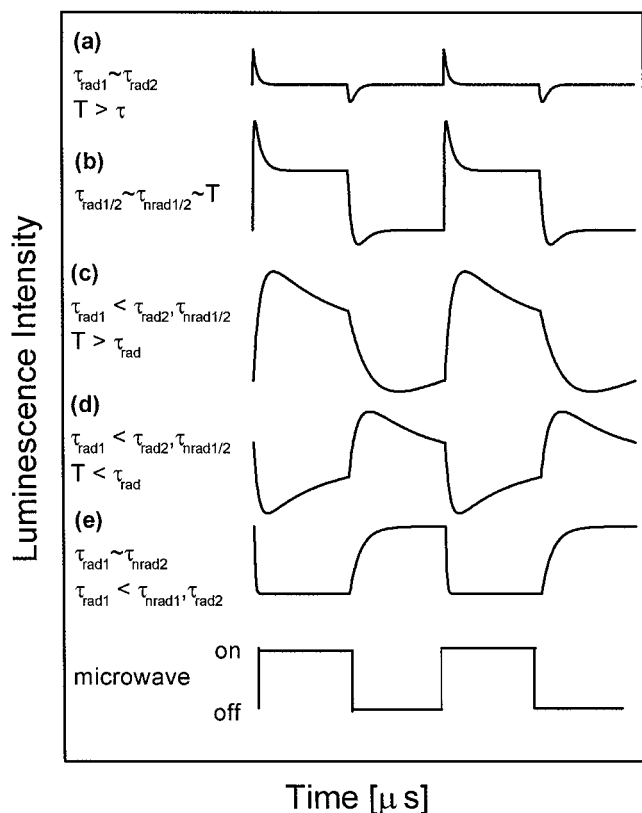


Figure 10. The simulated response of PL intensity to a square wave modulation of the MW power.

luminescence intensity response to be a mirror image of that shown in curve c, starting with a quenching of the luminescence intensity, followed by an enhancement at the falling edge. Curve e corresponds to a case dominated by nonradiative processes, characterized by a quenching of the luminescence intensity during the MW pulse. It can be seen from the curves in Figure 10, that thermalized and nonradiative processes lead to a quenching of the luminescence events, while unthermalized cases with dominate radiative effects, show mainly a spike with a gradual decay after the microwave pulse. The experimental TR-ODMR spectrum, shown in Figure 7, resembles the response shown in curves b or c of Figure 10. Indeed, the TR-ODMR was simulated with $\tau_{\text{rad}1} = 100 \mu\text{s}$, $\tau_{\text{nrad}1/2} = 800 \mu\text{s}$, $\tau_{\text{rad}2} \gg \tau_{\text{rad}1}$, and $T_1 = 250 \mu\text{s}$, as shown by the solid smooth line in Figure 7. This simulation suggests that the defect-to-band recombination is a radiative process, involving trapping of an electron at a phosphorus vacancy. In addition, the ODMR dependence on the MW modulation frequency, shown in Figure 6, is correlated with the transient time ODMR measurements by a Fourier transform. Accordingly, the frequency ODMR response was simulated with the TR-ODMR parameters (τ_{rad} , τ_{nrad} , and T_1) and shown by the solid lines in Figure 6. The fit of the theoretical curve with the experimental points is relatively good until about 4.5 kHz, but shows a large deviation above this frequency. The latter deviation cannot be explained at the current moment.

Summary

InP NCs prepared by colloidal techniques were investigated. The research was focused on the characterization of a defect luminescence band. Cw and TR-ODMR spectroscopy was utilized in combination with conventional luminescence technique. The ODMR spectrum consists of a single broad positive

resonance composed of left and right circular polarized components, mutually shifted by 0.008 T in a Faraday configuration. The defect luminescence was identified as a recombination of a valence band hole, with total angular momentum of $3/2$, and an electron trapped at a Vp site, with total angular momentum of $1/2$. The nonetched samples are dominated by Vp sites at the surface, while the etched samples are left with a small percent of vacancies at the core. The TR-ODMR measurements revealed characteristic decay times of about $100 \mu\text{s}$ for the radiative and about $800 \mu\text{s}$ for nonradiative spin levels. This measurement also revealed a spin-lattice relaxation is about $250 \mu\text{s}$.

Acknowledgment. This project was supported by the USA-Israel Binational Science foundation, contract no. 1999226. O. I. Micic and A. J. Nozik were supported by U. S. Department of Energy, Office of Science, Division of Chemical Sciences.

References and Notes

- (1) Alivisatos, A. P. *J. Phys. Chem.* **1996**, *100*, 13266 and references therein.
- (2) Fendler, J. H.; Meldrum, F. *Adv. Mater.* **1995**, *7*, 607.
- (3) Efros, A. L.; Rosen, M.; Kuno, M.; Nirmal, M.; Norris, D. J.; Bawendi, M. G. *Phys. Rev. B* **1996**, *53*, 4843.
- (4) Nirmal, M.; Norris, D. J.; Kuno, M.; Bawendi, M. G.; Efros, A. L.; Rosen, M. *Phys. Rev. Lett.* **1995**, *75*, 3728.
- (5) Schmitt-Rink, S.; Miller, D. A. B.; Chemla, D. S. *Phys. Rev. B* **1987**, *35*, 8113.
- (6) (a) Brus, L. E. *J. Phys. Chem.* **1984**, *80*, 4403. (b) Brus, L. E. *IEEE J. Quantum Electron.* **1986**, *QE-22*, 1909. (c) Brus, L. E. *J. Phys. Chem.* **1986**, *90*, 2555.
- (7) Giessen, H.; Fluegel, B.; Mohs, G.; Peyghambarian, N.; Spargue, J. R.; Micic, O. I.; Nozik, A. J. *Appl. Phys. Lett.* **1996**, *68*, 304.
- (8) Banin, U.; Bruchez, M.; Alivisatos, A. P.; Ha, T. J.; Weiss, S.; Chemla, D. S. *J. Chem. Phys.* **1999**, *110*, 1195.
- (9) Norris, D.; Bawendi, M. *Phys. Rev. B* **1996**, *53*, 16338.
- (10) Bertram, D.; Micic, O.; Nozik, A. *Phys. Rev. B* **1998**, *57*, R4265.
- (11) Williamson, A. J.; Zunger, A. *Phys. Rev. B* **1999**, *59*, 15819.
- (12) Bertram, D.; Micic, O. I.; Nozik, A. J. *Phys. Rev. B* **1998**, *57*, R4265.
- (13) Banin, U.; Lee, J. C.; Guzeliyan, A. A.; Kadavanich, A. V.; Alivisatos, A. P. *Superlattices Microstruct.* **1997**, *22*, 559.
- (14) Micic, O. I.; Cheong, H. M.; Fu, H.; Zunger, A.; Sprague, J. R.; Mascarenhas, A.; Nozik, A. J. *J. Phys. Chem. B* **1997**, *101*, 4904.
- (15) Bertram, D.; Hanna, M. C.; Nozik, A. J. *Appl. Phys. Lett.* **1999**, *74*, 2666.
- (16) (a) Fu, H.; Zunger, A. *Phys. Rev. Lett.* **1998**, *80*, 5397. (b) Fraceschetti, A.; Wang, L. W.; Fu, H.; Zunger, Z. *Phys. Rev. B* **1998**, *58*, R13367.
- (17) Micic, O. I.; Sprague, J.; Lu, Z.; Nozik, A. J. *Appl. Phys. Lett.* **1996**, *68*, 3150.
- (18) Poles, E.; Selmarten, D. C.; Micic, O. I.; Nozik, A. J. *Appl. Phys. Lett.* **1999**, *75*, 971.
- (19) Fu, H.; Zunger, A. *Phys. Rev. B* **1997**, *56*, 1496.
- (20) Micic, O. I.; Jones, K. M.; Cahill, A.; Nozik, A. J. *J. Phys. Chem., B* **1998**, *102*, 9791.
- (21) Murray, C. B.; Norris, D. J.; Bawendi, M. G. *J. Am. Chem. Soc.* **1993**, *115*, 8706.
- (22) Lifshitz, E.; Glozman, A.; Litvin, I. D.; Porteanu, H. *J. Phys. Chem. B* **2000**, *104*, 10449.
- (23) Lifshitz, E.; Bykov, L.; Yassen, M. *J. Phys. Chem.* **1995**, *99*, 15262.
- (24) Efros, A. Unpublished results.
- (25) von Bardeleben, H. J. *Solid State Commun.* **1986**, *57*, 137.
- (26) Boulitrop, F. *Phys. Rev. B* **1983**, *28*, 6192.
- (27) Chen, Y.; Gil, B.; Mathieu, H.; Lascaray, J. P. *Phys. Rev. B* **1987**, *36*, 1510.